Materialia 11 (2020) 100731

Contents lists available at ScienceDirect

Materialia

journal homepage: www.elsevier.com/locate/mtla

Full Length Article

Revealing the deformation mechanisms for room-temperature compressive superplasticity in nanocrystalline magnesium

Xin Wang[a,*], Lin Jiang[a,d], Dalong Zhang[a,e], Timothy J. Rupert[a], Irene J. Beyerlein[b], Subhash Mahajan[c], Enrique J. Lavernia[a], Julie M. Schoenung[a]

[a] Department of Materials Science and Engineering, University of California-Irvine, 92697, CA, USA
[b] Mechanical Engineering Department, Materials Department, University of California-Santa Barbara, 93106, CA, USA
[c] Department of Materials Science and Engineering, University of California-Davis, 95616, CA, USA
[d] Materials & Structural Analysis, Thermo Fisher Scientific, 97124, OR, USA
[e] Pacific Northwest National Laboratory, 99354, WA, USA

ARTICLE INFO

Keywords:
Nanocrystalline
Mg
Powder metallurgy
Deformation behavior
Strain rate sensitivity

ABSTRACT

Bulk nanocrystalline (NC) Mg processed by cryomilling of commercially pure Mg powder particles followed by spark plasma sintering exhibits a compressive strain >120% at room temperature. Compressive tests at strain rates ranging from 10^{-4} to 10^{-1} s^{-1} reveal a strain rate sensitivity (m) of ~0.17. Microstructural investigation reveals grain boundary migration accompanied with the ultra-large plastic deformation, which, along with the analysis of the deformation kinetics, deformation texture and dislocation structure, suggests that the excellent compressive plasticity in NC Mg mainly originates from grain boundary meditated deformation mechanisms and basal slip-dominated dislocation glide.

1. Introduction

Mg and its alloys offer promising potential for weight saving in lightweight engineering designs, such as in the automotive and aerospace industries [1, 2]. However, Mg is brittle at room temperature, a behavior that originates from the insufficient number of available deformation modes in the hexagonal close-packed (HCP) structure [3]. Elevated temperature can help activate more deformation modes, including slip on the HCP pyramidal planes [4-6], and is often required for mechanical processing of Mg structural components to avoid crack formation [7]. This substantially increases the manufacturing cost, accelerates the surface oxidation, and limits their application.

Superplastic forming has been proposed as an approach to simplify manufacturing and has been achieved in some intrinsically hard-to-form metals with reduced (<10 μm) grain size [8,9]. Important in this type of superplastic behavior are grain boundary mediated mechanisms, which occur usually at relatively high homologous temperatures ($T > 0.5\ T_m$, T_m is the melting temperature) and low strain rates ($<10^{-3}$ s^{-1}) when diffusive flow is reasonably rapid [10–12]. Many approaches have been employed to promote superplasticity at lower temperatures and/or higher strain rates, including: alloying to reduce the melting temperature at eutectic compositions [13], segregation at grain boundaries to enhance the grain boundary diffusivity [14], and, most commonly, refining the crystallite size [8-10,14-18]. Room temperature superplasticity has been reported in fine grained pure Mg [10] and Mg-Li alloys [14] processed via severe plastic deformation (SPD) of ingots.

For this reason, various research efforts have focused on extrapolating this grain size effect of superplasticity into the nanocrystalline (NC) regime [8,9,19,20]. However, this extrapolation is not straightforward. Divergent observations, ranging from extremely poor ductility (<5%) to excellent ductility or even superplasticity at ambient temperatures, have been reported in NC metals [21]. Data on NC HCP metals, in particular, is limited, and conflicting results, and incomplete explanations, still remain. For example, some studies have shown that the strain rate sensitivity in NC Mg [22], Ti [23] and Zn [24] is much larger than their coarse grained counterparts, while an opposite trend has also been reported for Ti [25, 26]. The deformation mechanisms of NC HCP metals are under debate. In addition, due to the anisotropic slip systems on the basal, prismatic and pyramidal planes in the HCP structure, the activity of various slip systems, if any, in NC HCP metals is still unclear. Direct microstructural evidence is needed to understand the plasticity in HCP metals, especially when their grain size enters the NC regime.

In light of the aforementioned knowledge gap, the purpose of this research study is to provide a detailed microstructural investigation into the deformation modes in bulk NC HCP Mg, in an effort to clearly explain the superplastic behavior observed in this material. Superplastic bulk NC Mg samples were synthesized using a “bottom-up” high energy mechanical milling approach, coupled with spark plasma sintering

* Corresponding author.
E-mail address: xin.wang@uci.edu (X. Wang).

https://doi.org/10.1016/j.mtla.2020.100731
Received 4 February 2020; Accepted 16 May 2020
Available online 19 May 2020

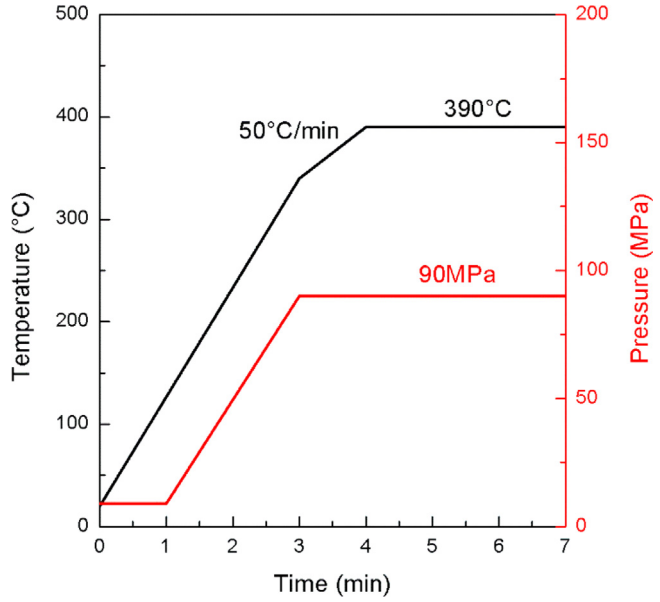

Fig. 1. Temperature and compaction pressure profiles during spark plasma sintering of cryomilled Mg powder.

(SPS), which has been effectively used to synthesize NC Mg and its alloys in previous studies [4,27]. Compressive tests were carried out at room temperature and at different strain rates, and an analysis of the strain rate sensitivity and activation volume was performed to evaluate the rate controlling mechanisms for plastic deformation. Through systematic microstructural and texture characterization, we found both basal slip and grain boundary mediated mechanisms play a significant role in the deformation behavior of NC Mg.

2. Experimental procedure

To synthesize the bulk NC Mg samples, commercially pure Mg powder particles (99.8%, 325 mesh, Alfa-Aesar) were cryomilled using a modified Szegvari-type attritor for 8 hours in flowing liquid argon. Stainless steel balls, 6.4 mm in diameter, were used as the attrition media, with a ball-to-powder weight ratio of approximately 30:1. Cryomilled Mg powder was loaded into a 20 mm inner diameter graphite die and consolidated into bulk samples by SPS (SPS-825S DR. SINTER, SPS Syntex Inc., Japan). Powders were sintered under vacuum at a sintering temperature of 390°C with a holding time of 3 min and a 90 MPa uniaxial compression pressure. Fig. 1 shows a typical temperature and compaction pressure profile as a function of time during SPS.

Compressive cuboids with dimensions of 4 × 4 × 6 mm were machined using electrical discharge machining such that the compressive direction was parallel to the SPS compaction axis. Compression tests were performed at room temperature using a servohydraulic testing machine operating under displacement control mode. To study the strain rate sensitivity, the bulk NC Mg samples were compressed at various strain rates of 10^{-4}, 10^{-3}, 10^{-2} and 10^{-1} s^{-1}. Compression tests performed at or below 10^{-2} s^{-1} were manually stopped when true strain reached ~120% because the samples did not fracture during compression. In the compression tests, molybdenum lubricant was used to minimize the friction between the samples and compression platens.

Microstructure and elemental composition of the cryomilled powder particles and the bulk NC Mg samples were characterized using an X-ray diffractometer (XRD, Smartlab, Rigaku, Cu Kα radiation), a scanning electron microscope (SEM, XL 30, FEI) equipped with an energy dispersive spectroscopy detector (EDS, Oxford Instruments) and an electron backscatter diffraction system (EBSD, HKL Technology), and transmission electron microscopes (TEM, CM20, FEI/Philips and JEM-2100, JEOL). In-plane XRD pole figures were measured for the bulk NC Mg samples before and after deformation for strain values up to 30%. The sample surfaces being diffracted were perpendicular to the compression axis. For TEM observation, cryomilled powder particles were mixed with an epoxy resin and cured at room temperature. TEM and transmission Kikuchi diffraction (TKD) specimens were prepared by mechanical grinding and ion milling. To prepare the deformed sample for TEM and transmission Kikuchi diffraction (TKD), the sample was first sectioned parallel to the compression axis by electrical discharge machining into thin foils ~1 mm in thickness. TEM and TKD images are therefore taken in a direction that is nominally parallel to the compression axis. The thin foil was then polished down to ~100 μm in thickness using diamond suspensions. Finally, ion milling was used to prepare electron transparent specimens. The operation of slip systems was determined by TEM diffraction contrast analysis in a bulk NC Mg sample compressed to 30% strain (hereafter designated as 30%Mg).

3. Results and discussion

Fig. 2 shows the morphology and nanocrystalline microstructure of the cryomilled Mg powder particles. The cryomilled powders consist of faceted and close-to-equiaxed particles, with an average particle size of ~11.1 μm, as illustrated by a representative SEM secondary-electron micrograph shown in Fig. 2(a) and the corresponding particle size distribution plotted in Fig. 2(b). A detailed discussion on the evolution of powder morphology during 8 hours of cryomilling can be found in [28]. The bright field and dark field TEM micrographs of the cryomilled powder particles in Fig. 2(c) and (d) show the formation of NC grains, with an average grain size of approximately 50 nm and irregular grain morphology.

After SPS, the relative density of the bulk NC Mg samples measured by the Archimedes method was ~99.6%. SEM EDS analysis (Fig. 3) reveals O (~3.5 wt%) and Ar (~1.9 wt%) contamination in the bulk NC Mg, possibly originated from the atmosphere and the cryomilling media. TEM images in Fig. 4(a) and (b) show a NC structure with a nearly equiaxed grain morphology. A statistical distribution of grain diameters (Fig. 4(c)) was measured from the TEM images, showing a narrow grain size distribution in which ~85% of the grains are smaller than 100 nm and ~3.2% of the grains have diameters larger than 200 nm, with the average grain size being ~74 nm.

Quantitative XRD analysis (Fig. 5) using the Williamson-Hall Method [29] yielded average grain sizes for the cryomilled powder and the bulk NC Mg of 46 ± 4 nm and 61 ± 2 nm, respectively, and microstrain values of (2.17 ± 0.17) × 10^{-3} and (3.82 ± 0.35) × 10^{-4}, respectively. Grain coarsening is limited during sintering as SPS allows higher heating rates and shorter holding time compared to conventional hot pressing. A high microstrain (often induced by dislocations, faults and other defects) is typically observed in cryomilled powders, as a result of high-energy ball milling and the suppressed dynamic recovery at cryogenic temperature [30, 31]. The microstrain decreases after sintering due to recovery and recrystallization at the relatively high sintering temperature (~0.72 T_m).

The results of the uniaxial compression tests at strain rates of 10^{-4} to 10^{-1} s^{-1} are shown in Fig. 6(a). The compressive stress strain curves are characterized by strain hardening at low strain, which leads to early peaks in stress, followed by slight softening and then a region of nearly constant flow stress with increasing strain. The lack of sustained strain hardening indicates restricted accumulation of intragranular dislocations and twins, both of which would yield apparent strain hardening, at large strain. The 0.2% offset compressive yield stress ($\sigma_{0.2\%}$) increases from ~80 MPa at a strain rate of 10^{-4} s^{-1} to ~260 MPa at a strain rate of 10^{-1} s^{-1}. Compared to coarse-grained wrought Mg, which usually exhibits a strain below ~30% during room temperature compression [32-34], the bulk NC Mg in this study showed an exceptionally high compressive strain-to-failure, larger than 120% at strain rates at or below 10^{-2} s^{-1}. Even at a high strain rate of 10^{-1} s^{-1}, the samples did not

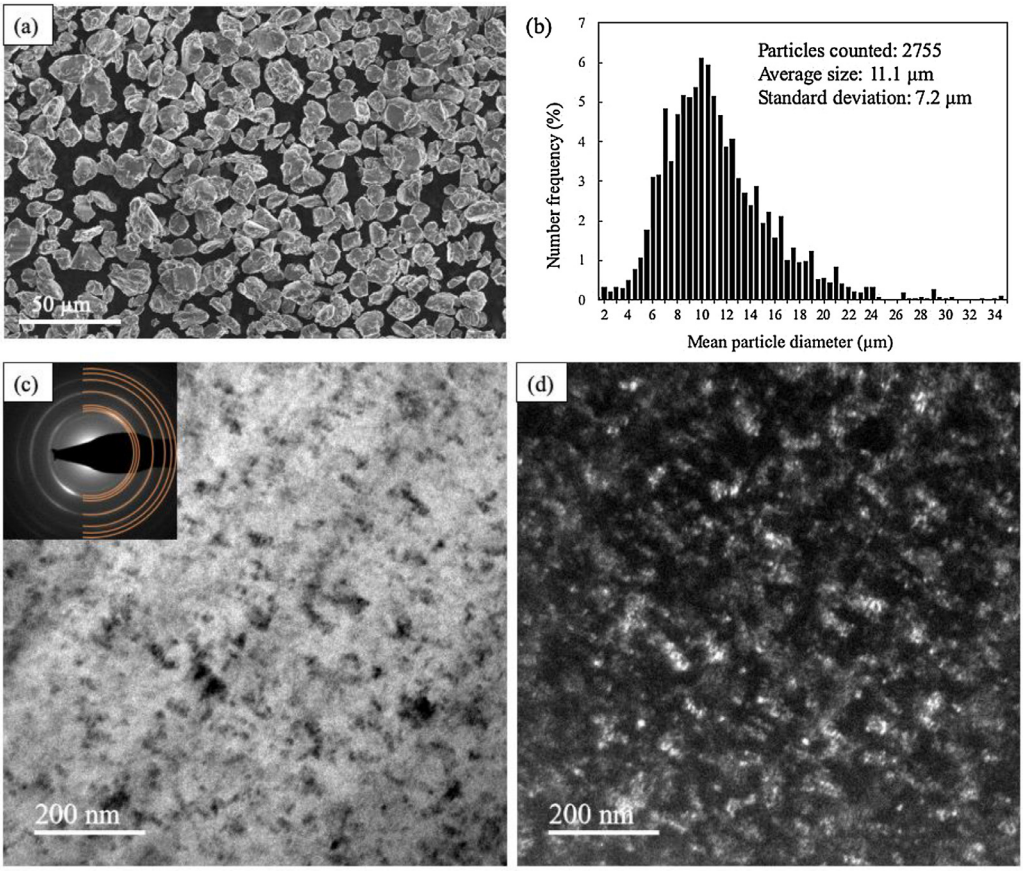

Fig. 2. Cryomilled Mg powder particles: (a) representative SEM image; (b) histogram of the mean particle diameter distribution; (c) and (d) TEM bright and dark field images.

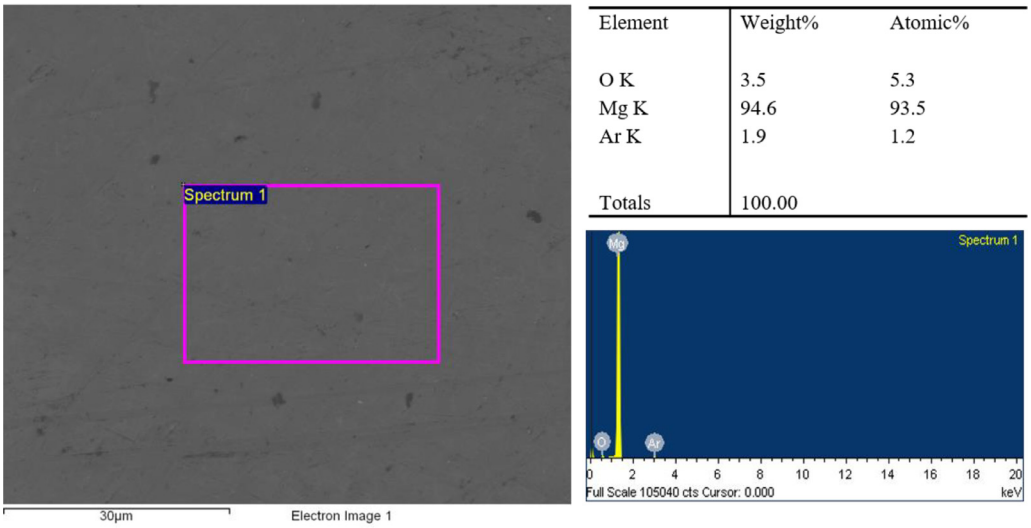

Element	Weight%	Atomic%
O K	3.5	5.3
Mg K	94.6	93.5
Ar K	1.9	1.2
Totals	100.00	

Fig. 3. SEM energy dispersive spectroscopy (EDS) spectrum and the summary of chemical composition in the SPS-consolidated bulk NC Mg.

fracture after experiencing compressive strain of ~60%. In addition, the compressive deformation is largely uniform without shear banding.

To elucidate the origin of the high compressive strain in the bulk NC Mg at room temperature, the strain rate sensitivity and activation volume were calculated. The strain rate sensitivity exponent, m, can be calculated from the yield stress - strain rate relationship,

$$m = \frac{\partial \ln \sigma}{\partial \ln \dot{\varepsilon}} \quad (1)$$

where σ is the yield stress and $\dot{\varepsilon}$ is the strain rate. The 0.2% offset yield stress values ($\sigma_{0.2\%}$) obtained in room temperature compression are plotted as a function of the strain rate in a double-logarithmic graph in Fig. 6(b). From the slope of the curve in Fig. 6(b), an m value of ~0.17 was calculated. The activation volume V^* can then be calculated using,

$$V^* = \frac{\sqrt{3}kT}{\sigma m} \quad (2)$$

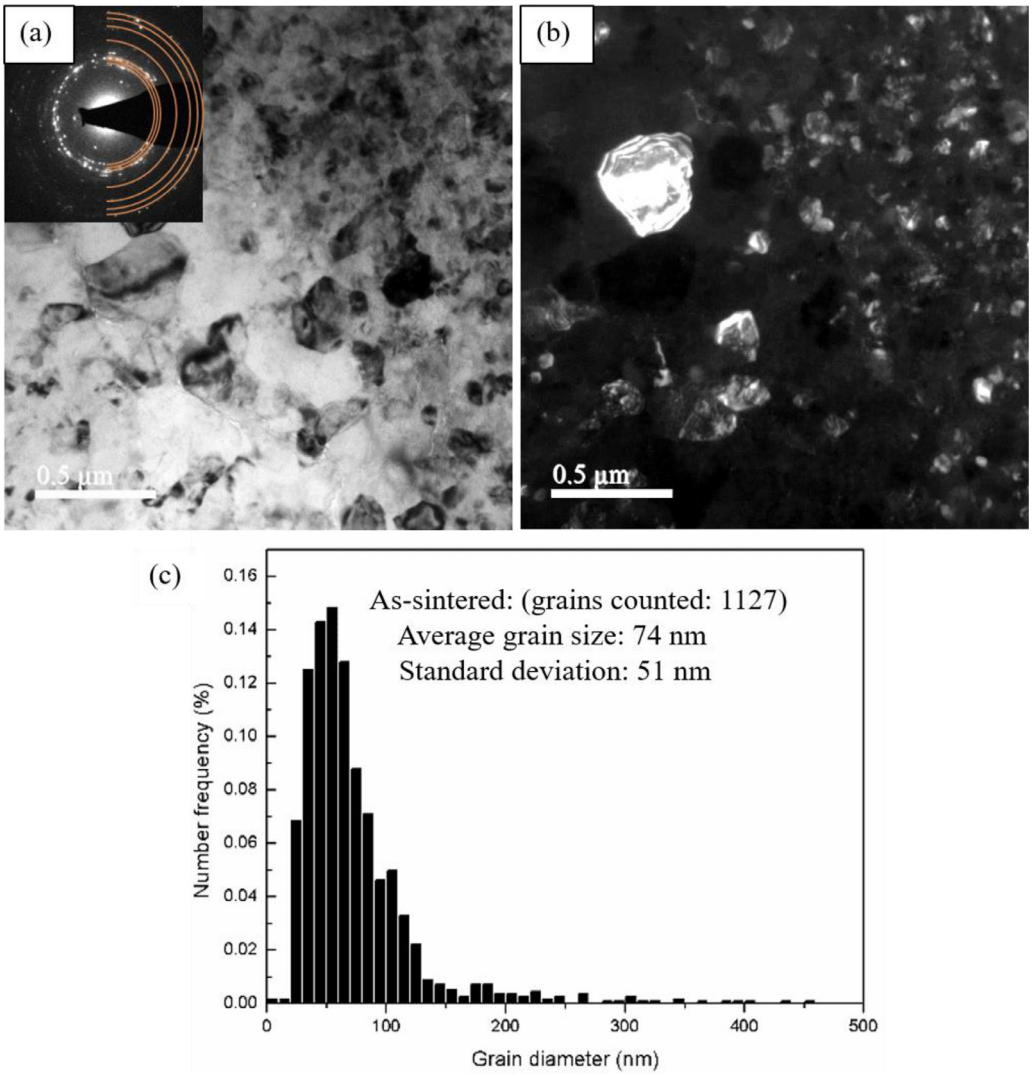

Fig. 4. Bulk nanocrystalline Mg: (a) and (b) TEM bright and dark field images; (c) histogram of the grain size distribution measured from the TEM images.

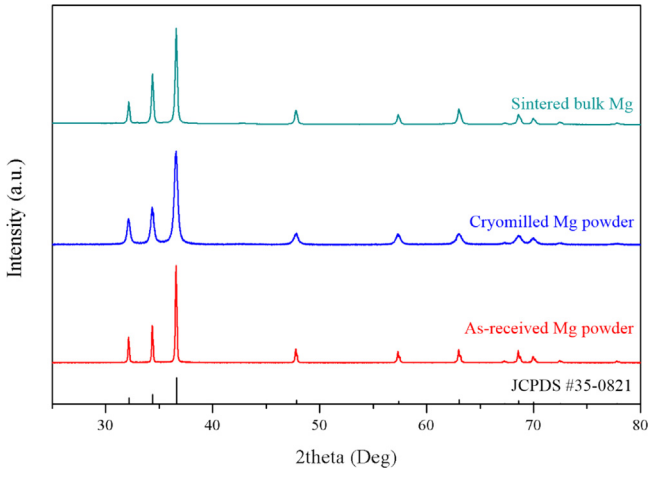

Fig. 5. XRD patterns for the as-received Mg, cryomilled Mg powder particles, and SPS-consolidated bulk NC Mg samples.

where k is the Boltzmann constant ($k = 1.38 \times 10^{-23}$ J/K) and T is absolute temperature (T = 300 K). The activation volume was calculated to be ~10.7 b^3, where b is the value of the Burgers vector for basal slip in Mg. For coarse-grained Mg deformed at room temperature, the activation volume is much higher (~400 b^3) [35]. The difference arises because in traditional Mg comprised of much larger grain sizes, the primary deformation mechanisms are obstacle formation by the storage of forest dislocations within the grains and dislocation-grain boundary and dislocation-twin boundary interactions. When grain boundary sliding dominates, the activation volumes decrease substantially. For instance, in ultrafine grained Mg deformed at high temperatures, the activation volume of ~1 b^3 has been reported [35]. In the bulk NC Mg in the present study, an intermediate value for the activation volume is observed, suggesting a combination of deformation mechanisms, as revealed by the microstructural characterization below. The strain hardening capability of the samples quickly saturated at a low strain level below 10%, which is typical in NC materials with limited activation of intragranular dislocation slip [36,37]. Such an inadequate strain hardening capacity often leads to localized deformation (i.e., necking) and poor ductility in NC materials under tensile deformation, despite a large uniform strain observed in compression. However, the relatively high value for the strain rate sensitivity, m value, as seen here for the NC Mg at room temperature, may help stabilize a uniform deformation. Due to the limited sample size, tensile tests cannot be performed in the present study. Further investigation is needed to thoroughly understand the tensile behavior of this material.

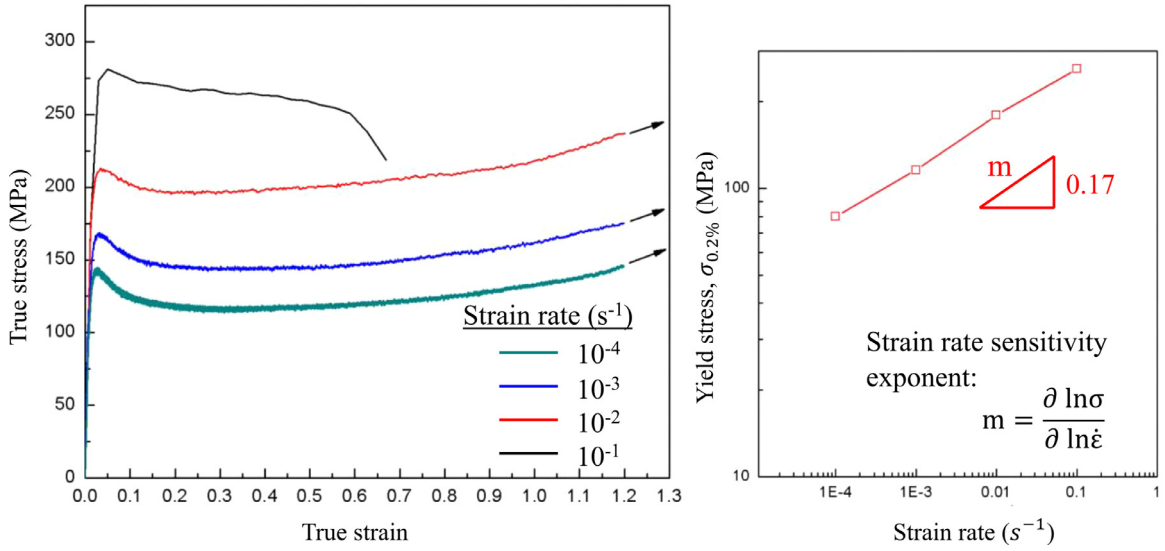

Fig. 6. (a) True stress-strain curves for bulk NC Mg under compression at room temperature and various strain rates; (b) double-log plot of yield stress versus strain rate.

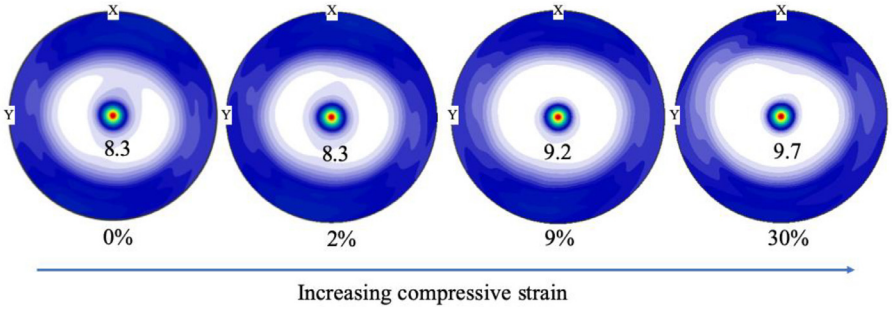

Fig. 7. Pole figures showing the texture evolution during compression of the bulk NC Mg at increasing strain levels. The inset number is the peak intensity for each pole figure in the unit of multiples of uniform distribution (m.u.d.).

To probe the deformation mechanisms that are responsible for the small activation volume being obtained in the bulk NC Mg sample, the texture evolution during compression at a moderate strain rate of 10^{-3} s^{-1} was examined in detail. Fig. 7 shows the (0001) pole figures measured on the Mg sample in the as-sintered state and after 2%, 9% and 30% room-temperature compressive strain. The sample exhibits a basal texture with the basal pole parallel to the SPS compaction axis, which is also the compression direction. The peak texture intensity in the unit of multiple of uniform distribution (m.u.d.) is indicated in each pole figure. Although the main character of basal texture remained the same during deformation, the intensity of this basal texture slightly increases with an increasing strain from 8.3 m.u.d. in the as-sintered sample to 9.7 m.u.d. after deformation to ~30% strain. The primary activation of basal slip and/or $\{10\bar{1}2\}$ deformation twinning would generate an increment in the basal texture intensity that is observed here, while non-basal slip modes would lead to off-basal texture.

Post-mortem TEM was also performed on sample 30%Mg to reveal the microstructure after deformation. TEM bright-field images of 30%Mg are shown in Fig. 8. TEM results reveal that dislocation slip is a primary deformation mechanism. Although less frequently found in grains smaller than 100 nm in diameter, dislocations were clearly observed in relatively large ultrafine grains. Different diffraction conditions were used to discern the types of dislocations, i.e., <**a**>, <**c**> and <**c+a**> types, in a representative ultrafine Mg grain with a grain size of ~550 nm. <**a**>, <**c**> or <**c+a**> represent the most commonly observed dislocations in Mg, with the Burgers vector b = $1/3\langle 11\bar{2}0\rangle$, <0001> and $1/3\langle 11\bar{2}3\rangle$, respectively. According to the **g•b ≠ 0** visibility criterion, where **b** is the Burgers vector and **g** is a diffraction vector, when **g** = $10\bar{1}0$ was used, most <**a**> and <**c+a**> dislocations can be observed; whereas, if **g** = 0002 is used, most <**a**> dislocations become invisible. Fig. 8(c) and (d) show the two-beam bright field and dark field micrographs, respectively, taken near the zone axis **B** = $[1\bar{2}10]$ with the diffraction vector **g** = $10\bar{1}0$. Further, most of the dislocations have lines of contrast along the basal plane trace, while some of them lie out of the basal planes. Dislocations parallel to the basal plane trace are marked by red arrows in the figure, and dislocations out of the basal planes are marked by green. Fig. 8(e) and (f) show the bright-field and dark-field micrographs, respectively, taken at the **g** = 0002 two-beam condition for the same sample region. The majority of dislocations lose contrast when **g** = 0002. The visible dislocations are highlighted in the figures with blue arrows. Combining the facts that a high density of dislocation lines was observed when **g** = $10\bar{1}0$, while only few dislocations were visible when g = 0002, it follows that most of the dislocations present in the ultrafine grains are <**a**> dislocations on the basal planes.

In addition, a few $\{10\bar{1}2\}$ deformation twins were detected by TKD in 30%Mg. As shown in the inverse pole figure (IPF) colored map in Fig. 9(a), $\{10\bar{1}2\}$ twin boundaries were marked by white circles. The grain boundary misorientation distribution is plotted in Fig. 9(b). An obvious peak is observed in the 85°-90° misorientation range. Inset in Fig. 9(b) is the inverse pole figure showing the distribution of rotation axes for grain boundaries with misorientation in the range of 86 ± 5°. The rotation axes cluster around $[\bar{1}2\bar{1}0]$, which is corresponding to the formation of $\{10\bar{1}2\}$ twin boundaries with a ~86°/ $[\bar{1}2\bar{1}0]$ twin-matrix misorientation relationship. Although $\{10\bar{1}2\}$ twins were observed, the fraction of twins in NC Mg at 30% strain is minimal compared to that normally observed in conventional coarse-grained Mg after small strain along directions that favor twin formation. For instance, the area fraction of $\{10\bar{1}2\}$ twins reaches 42% after only 3% compressive strain along

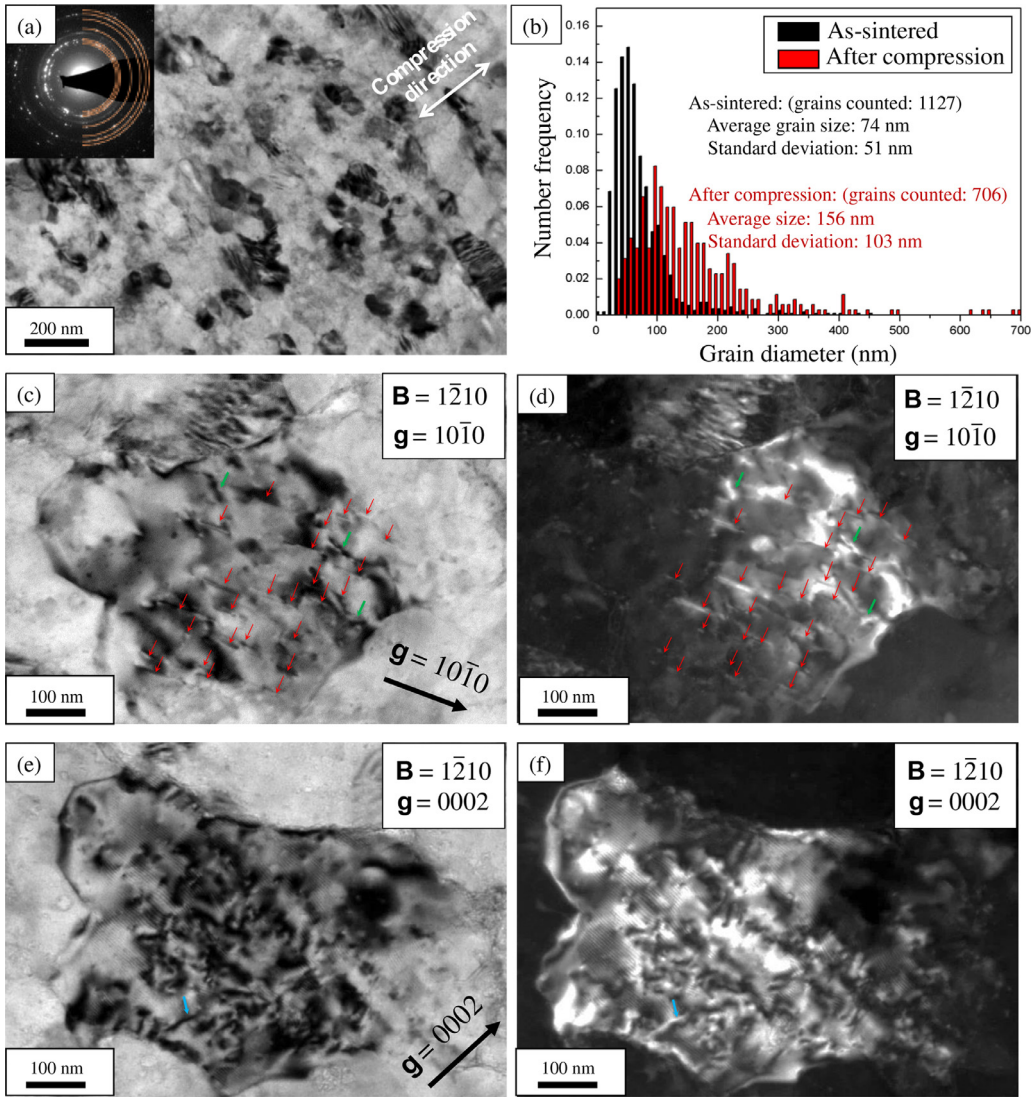

Fig. 8. (a) TEM image showing the microstructure of sample 30%Mg; (b) grain size distributions for the Mg sample before and after compression. Bright and dark field TEM images for sample 30%Mg at a grain near the zone axis B = [1$\bar{2}$10], when (c and d) the diffraction vector g = 10$\bar{1}$0 and (e and f) g = 0002.

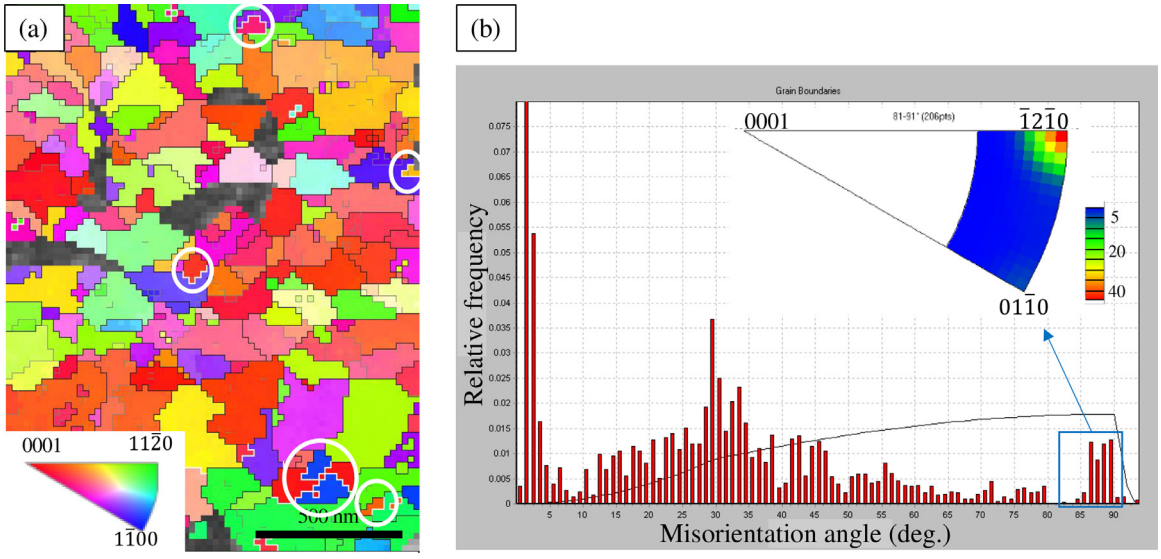

Fig. 9. (a) Transmission Kikuchi diffraction (TKD) map of sample 30%Mg and (b) the corresponding histogram of the grain boundary misorientation distribution (the insert is the inverse pole figure showing the distribution of rotation axes for grain boundaries with misorientation in the range of 86 ± 5°). A few {10$\bar{1}$2} twins were observed in 30%Mg, which are marked by white circles in (a).

the transverse direction in pre-rolled coarse-grained Mg [38]. The low occurrence of twins in NC Mg is in consistent with an absence of a stress plateau before strain hardening, which is characteristic of twinning, in the stress-strain curves (Fig. 6(a)). Therefore, the contribution of twins to the overall compressive strain in NC Mg is negligible, as the strain accommodated by twinning is proportional to the volume fraction of twins with a theoretical maximum of 6.5% [39].

Moreover, the grains in the deformed microstructure became coarsened and elongated in the direction perpendicular to the compression direction (Fig. 8(a)) after room temperature compression. The grain size statistics for 30%Mg, measured from the TEM micrographs, are plotted in Fig. 8(b), together with those for the as-sintered Mg sample. The average grain size increased from ~74 nm for the as-sintered sample to ~156 nm for 30%Mg, which is in agreement with previous investigations that have reported superplasticity and grain growth occurring concurrently as a result of strain-induced grain boundary migration [40]. The experimental finding that grain boundaries are mobile in NC Mg during room temperature compression and that the mobility is anisotropic relative to the compressive strain direction suggests that grain boundaries can actually accommodate plastic strain in addition to dislocation slip and deformation twinning. Furthermore, grain growth in NC Mg caused by strain-induced grain boundary migration explains the softening observed in the stress-strain curves (Fig. 6(a)), since this phenomenon can make the activation of dislocation slip easier [41].

In coarse-grained pure Mg with basal texture, when compressed parallel to its basal pole, the strain along the c-axis needs to be accommodated by slip with non-basal Burgers vectors [39]. Under this deformation condition, Mg samples usually exhibit strong work hardening, accompanied by a low strain-to-failure at temperatures below 200°C [42]. This phenomenon has recently been correlated to the anomalous basal dissociation behavior of the <**c+a**> dislocations [42]. In contrast, in the NC Mg sample with a basal texture, in the current study, TEM diffraction analysis suggests the scarcity of <**c+a**> dislocations and twins after c-axis compression. Although a fair number of basal dislocations have been observed in the deformed microstructure in Fig. 8(c, d), basal slip alone cannot accommodate the high compressive strain being observed. In addition, an overall strain softening soon after yielding was observed in the NC Mg sample, indicating the suppression of <**c+a**> dislocation slip and the activation of grain boundary mediated mechanisms as alternative deformation modes [43, 44]. Furthermore, the presence of magnesium oxides, as a result of the powder metallurgy processing, may also contribute to the increased strain rate sensitivity observed in NC Mg. However, the effect of possible reinforcement phase-induced constraints is negligible when compared to the effect of grain boundaries in NC Mg, considering the high-volume fraction of grain boundaries and the relatively low concentration of oxygen.

4. Conclusions

Bulk NC Mg was fabricated by cryomilling and SPS in the present study. A large, superplastic strain of ~120% was observed during compression at room temperature with a strain rate up to 10^{-2} s^{-1}. NC Mg with an average grain size of 74 nm shows an increased strain rate sensitivity with m = ~0.17 compared to coarse grained Mg at room temperature. Texture evolution and TEM analysis were used to determine the activation behavior of different types of dislocations in NC Mg. Enhanced grain boundary mediated activity together with basal slip were determined to be the major contributors to the deformation mechanisms for the large compressive strain observed at room temperature.

Declaration of interest

The authors declare no competing financial interests.

Acknowledgments

The authors acknowledge financial support from the National Science Foundation (NSF CMMI-1729829, NSF CMMI-1729887, and NSF CMMI-1723539).

References

[1] M.K. Kulekci, The International Journal of Advanced Manufacturing Technology 39(9) (2008) 851-865.
[2] T.M. Pollock, Science 328 (5981) (2010) 986–987.
[3] J.P. Hirth, J. Lothe, Theory of Dislocations, McGraw-Hill1967.
[4] M. Pozuelo, C. Melnyk, W.H. Kao, J.-M. Yang, J. Mater. Res. 26 (7) (2011) 904–911.
[5] A. Chapuis, J.H. Driver, Acta Mater. 59 (5) (2011) 1986–1994.
[6] C.M. Cepeda-Jiménez, J.M. Molina-Aldareguia, M.T. Pérez-Prado, Acta Mater. 88 (2015) 232–244.
[7] S.R. Agnew, P. Mehrotra, T.M. Lillo, G.M. Stoica, P.K. Liaw, Acta Mater. 53 (11) (2005) 3135–3146.
[8] S.X. McFadden, R.S. Mishra, R.Z. Valiev, A.P. Zhilyaev, A.K. Mukherjee, Nature 398 (6729) (1999) 684–686.
[9] L. Lu, M.L. Sui, K. Lu, Science 287 (5457) (2000) 1463–1466.
[10] R.B. Figueiredo, S. Sabbaghianrad, A. Giwa, J.R. Greer, T.G. Langdon, Acta Mater 122 (2017) 322–331.
[11] Z. Zeng, J.-F. Nie, S.-W. Xu, C.H.J. Davies, N. Birbilis, Nat. Commun. 8 (1) (2017) 972.
[12] J. Koike, R. Ohyama, T. Kobayashi, M. Suzuki, K. Maruyama, Mater. Trans. 44 (4) (2003) 445–451.
[13] A.E. Geckinli, C.R. Barrett, J. Mater. Sci. 11 (3) (1976) 510–521.
[14] K. Edalati, T. Masuda, M. Arita, M. Furui, X. Sauvage, Z. Horita, R.Z. Valiev, Scientific Reports 7 (1) (2017) 2662.
[15] Z. Horita, K. Matsubara, K. Makii, T.G. Langdon, Scr. Mater. 47 (4) (2002) 255–260.
[16] K. Matsubara, Y. Miyahara, Z. Horita, T.G. Langdon, Acta Mater. 51 (11) (2003) 3073–3084.
[17] D. Pan, S. Kuwano, T. Fujita, M.W. Chen, Nano Letters 7 (7) (2007) 2108–2111.
[18] J. Li, W. Xu, X. Wu, H. Ding, K. Xia, Materials Science and Engineering: A 528 (18) (2011) 5993–5998.
[19] R.S. Mishra, S. McFadden, A.K. Mukherjee, Materials Science Forum 304-306 (1999) 31–38.
[20] J.R. Weertman, D. Farkas, K. Hemker, H. Kung, M. Mayo, R. Mitra, H.V. Swygenhoven, MRS Bulletin 24(2) (2013) 44-53.
[21] M.A. Meyers, A. Mishra, D.J. Benson, Prog. Mater. Sci 51 (4) (2006) 427–556.
[22] S. Hwang, C. Nishimura, P.G. McCormick, Scr. Mater. 44 (8) (2001) 1507–1511.
[23] F. Wang, B. Li, T.T. Gao, P. Huang, K.W. Xu, T.J. Lu, Surface and Coatings Technology 228 (2013) S254–S256.
[24] X. Zhang, H. Wang, R.O. Scattergood, J. Narayan, C.C. Koch, A.V. Sergueeva, A.K. Mukherjee, Acta Mater. 50 (19) (2002) 4823–4830.
[25] D. Jia, Y.M. Wang, K.T. Ramesh, E. Ma, Y.T. Zhu, R.Z. Valiev, Appl. Phys. Lett 79 (5) (2001) 611–613.
[26] Q. Wei, J. Mater. Sci 42 (5) (2007) 1709–1727.
[27] B. Zheng, O. Ertorer, Y. Li, Y. Zhou, S.N. Mathaudhu, C.Y. Tsao, E.J. Lavernia, Materials Science and Engineering: A 528 (4-5) (2011) 2180–2191.
[28] X. Wang, L. Jiang, D. Zhang, I.J. Beyerlein, S. Mahajan, T.J. Rupert, E.J. Lavernia, J.M. Schoenung, Acta Mater 146 (2018) 12–24.
[29] G.K. Williamson, W.H. Hall, Acta Metallurgica 1 (1) (1953) 22–31.
[30] D.B. Witkin, E.J. Lavernia, Prog. Mater. Sci. 51 (1) (2006) 1–60.
[31] H. Wen, T.D. Topping, D. Isheim, D.N. Seidman, E.J. Lavernia, Acta Mater 61 (8) (2013) 2769–2782.
[32] S.R. Agnew, M.H. Yoo, C.N. Tomé, Acta Mater. 49 (20) (2001) 4277–4289.
[33] M.R. Barnett, M.D. Nave, C.J. Bettles, Materials Science and Engineering: A 386 (1) (2004) 205–211.
[34] M.D. Nave, M.R. Barnett, Scr. Mater. 51 (9) (2004) 881–885.
[35] H.J. Choi, Y. Kim, J.H. Shin, D.H. Bae, Materials Science and Engineering: A 527 (6) (2010) 1565–1570.
[36] J. Schiøtz, K.W. Jacobsen, Science 301 (5638) (2003) 1357–1359.
[37] J. Schiøtz, F.D. Di Tolla, K.W. Jacobsen, Nature 391 (1998) 561.
[38] I.J. Beyerlein, L. Capolungo, P.E. Marshall, R.J. McCabe, C.N. Tomé, Philos. Mag. 90 (2010) 2161–2190.
[39] S.R. Agnew, O. Duygulu, Int. J. Plast 21 (6) (2005) 1161–1193.
[40] D.S. Wilkinson, C.H. Cáceres, Acta Metallurgica 32(9) (1984) 1335-1345.
[41] T.J. Rupert, D.S. Gianola, Y. Gan, K.J. Hemker, Science 326 (5960) (2009) 1686.
[42] Z. Wu, W.A. Curtin, Nature 526 (2015) 62.
[43] Z. Shan, E.A. Stach, J.M.K. Wiezorek, J.A. Knapp, D.M. Follstaedt, S.X. Mao, Science 305 (5684) (2004) 654–657.
[44] H. Van Swygenhoven, Science 296 (5565) (2002) 66–67.